EPJ Web of Conferences **340**, 10019 (2025)
Powders & Grains 2025 https://doi.org/10.1051/epjconf/202534010019

Simulating the 3D photoelasticity forward problem in order to generate training images for deep learning

Peidong Yu[1,*], *Kianoosh* Taghizadeh[5,6], *Dorian Didier* Feisel[1,2,**], *Saswati* Ganguly[1,2], *Matthias* Schröter[3,4], and *Matthias* Sperl[1,2]

[1]Institut für Materialphysik im Weltraum, Deutsches Zentrum für Luft- und Raumfahrt (DLR), 51170 Cologne, Germany
[2]Institut für Theoretische Physik, Universität zu Köln, 50937 Cologne, Germany
[3]Max-Planck-Institut für Dynamik und Selbstorganisation, 37077, Göttingen, Germany
[4]Hypatia Science-Consulting, 37081, Göttingen, Germany
[5]Laboratoire Navier, École des Ponts ParisTech, Université Gustave Eiffel, CNRS, 77455 Marne-la-Vallée, France
[6]Department of Physics, Faculty of Science, Kyoto Sangyo University, 603-8555 Kyoto, Japan

Abstract. Images of two-dimensional granular packings obtained using photoelastic particles and a polariscope setup have successfully revealed inaccessible information such as inter-particle contacts, contact force distributions and force chain structures. Reproducing this success for a three-dimensional granular system requires a tomography setup and becomes therefore significantly more difficult. Most importantly, there is no analytical mathematical solution to the problem to reconstruct the three-dimensional stress field from the acquired images. Using a neural network to numerically predict the stress field could be a promising way forward. Training the network requires a dataset connecting photoelastic images with the knowledge of the internal stress state of the sample those images are taken from. Because the latter is not experimentally accessible, we describe here the framework of how to create the training data by simulating the forward problem of photoelasticity numerically with the following steps: simulation of stress tensor distribution within each particle given the contact forces, and simulation of photoelastic response (i.e., fringe patterns captured by a camera).

1 Introduction

The experimental technique of photoelasticimetry has been used to measure inter-particle contact forces in granular systems since 1950s [1]. The most prolific results yielded by this technique are from 2D granular systems consisted of disks made by photoelastic materials. In these 2D systems, the capability of measuring contact forces has enabled investigations on force distribution [2, 3], jamming transitions [4, 5], response to shear [6, 7], and dynamic behavior [8] of granulates. For 3D systems, fluorescent imaging and X-ray diffraction methods have been used to study contact forces [9, 10] from particle deformation. Photoelasticimetry is nevertheless still desired for its capability of measuring small forces with little deformation. However, several experimental challenges are encountered in 3D: the production of spherical photoelastic particles free of internal stresses, the need to index-match those particles to avoid refraction, and the acquisition of tomographic data. There have been several qualitative studies of 3D systems [11, 12]; most importantly Li *et al.* have successfully addressed all experimental problems and reconstructed the structure of the 3D force chains [13].

However, none of the existing 3D studies has reached the ultimate goal of photoelasticimetry: the measurement of inter-particle contact forces. The underlying reason is the lack of a mathematical tool to resolve the problem of tensor-field tomography. In 2D, the assumption of a constant stress tensor along the light path greatly reduces the difficulty of solving the so called *inverse problem*: calculation of stress tensors and contact force from light intensity data. For 3D systems, X-ray diffraction technique has been used to measure In 3D, this assumption no longer holds. Even provided with tomographic data of light intensity from various directions, the current progress in the mathematics community [14] still does not provide an analytical or numerical solution of the *inverse problem*.

The recent progress of machine learning, on the other hand, provides the option of performing 3D reconstruction from tomography data with the aid of deep learning [15, 16]. It is therefore reasonable to expect that a properly trained neural network can also learn to solve the *inverse problem* of photoelasticimetry. The difficulty here is to provide reliable input data (2D photoelastic images of 3D granular assemblies) and target data (the 3D stress distribution inside the particles) for the training. While the input data can be gathered from tomographic experiments with photoelastic particles, as shown e.g. in [13], there is no alternative method known to simultaneously measure the stress data.

The way forward are therefore simulations, which can perform all steps necessary to generate a full set of train-

---

[*] e-mail: peidong.yu@dlr.de
[**] e-mail: dorian.feisel@dlr.de

ing data: (1) calculate contact forces of a packing of particles, (2) calculate stress distribution inside a particle given the contact forces, and (3) calculate the light intensity of a photoelastic image of the packing at an arbitrary direction given the stress distribution in each particle. Together, the three steps form the solution of the *forward problem* which is needed to train a network to solve the *inverse problem*.

For the first step, existing software tools have enabled many simulation works, e.g. [17]. In the current work we focus on the last two steps. In the following sections, we introduce first the Finite Element Method (FEM) simulation to retrieve stress data, and then the photoelasticity theory needed for photoelastic calculation, and eventually the photoelastic simulation tool to generate example training images.

2 FEM simulation of stress data

To obtain stress propagation between two elastic spherical particles in contact, an FEM simulation is conducted using the commercial software Abaqus/CAE [18]. To simplify the geometry, we examine the equivalent problem of contact between rigid flats and an elastic particle. Taking advantage of symmetry, the sphere was modeled by a half circle with a diameter of d=10 mm, compressed between two analytical rigid flat surfaces. This model improves the computational efficiency significantly and allows a 2D axisymmetric simulation [19]. The particle is assumed to be homogeneous and isotropic following linear elastic material response with Young's modulus $E = 1.2$ MPa and Poisson ratio $\nu = 0.49$.

A compressive force, $F = 1$ N, is applied to a reference point. Movement of the reference point is coupled with the top flat surface which results in a uniform force applied on the top of the sphere. No constraint is imposed in the radial direction on the top edge to allow radial expansion as it would naturally occur in uniaxial compression. The nodes of the bottom flat are fixed in all directions to model the rigid flat. The nodes on the symmetry axis, z−axis, of the sphere are fixed in the radial direction to model a sphere. Contacts are modeled as frictionless in the tangential direction and hard in the normal direction (the tangent modulus and the friction coefficient assumed as zero). A mesh refinement study is conducted, leading to a mesh of 16,769 CAX4RH (4-node bilinear axisymmetric quadrilateral, reduced integration, hourglass control) elements used to discretize the sphere, with significantly increased mesh refinement along the curved contact edge where contact occurs. The mesh far from the contact edge became coarser to improve computing speed. The mesh and boundary conditions used are shown in Fig. 1(a).

Due to the contact nonlinearity and large deformation at the contact points, a large deflection was activated during the simulation. The simulation validation in the limit of small deformation was carried out in comparison to Hertzian law. The results (not shown here) compare well with the Hertz elastic solution with an error less than 1% [19]. Thanks to the symmetric nature of the problem, a 3D sphere is generated by rotating the 2D axisymmetric model 360°. Fig. 1(b) shows the z− component of stress tensor at the end of the simulation. Highest and lowest compressive stress in the sphere are marked in blue and red color respectively.

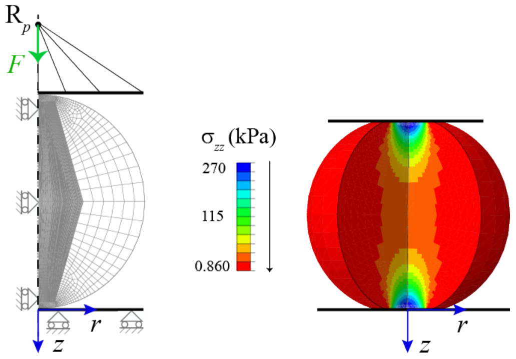

(a) (b)

Figure 1. (a) Finite element mesh and boundary conditions used for the simulation of spherical elastic particle between rigid flat surfaces/plates. (b) The z−component of the stress tensor σ_{zz} within the 3D sphere compressed under force $F = 1$ N.

3 Theory of integrated photoelasticity

In photoelasticimetry, a beam of light acts as the probe to the photoelastic particles of interest. Given that no refraction happens when the light enters or exits the boundaries of the particles, the polarization state of the probing light is affected by the stress distributed along its straight path due to the photoelastic effect (thus more precisely also called *stress-birefringence*). By using a device called the polariscope, the polarization state of the outgoing light, which carries the stress information along its path, is converted to the light intensity of a photoelastic image pixel.

For light beam propagating along the z axis, the Jones vector of the beam $\boldsymbol{E} = (E_x, E_y, 0)$ follows the Maxwell's equation for birefringent materials:

$$\begin{aligned} -\frac{d^2 E_x}{dz^2} &= \frac{\omega^2}{c^2}(\varepsilon_{xx}E_x + \varepsilon_{xy}E_y) \\ -\frac{d^2 E_y}{dz^2} &= \frac{\omega^2}{c^2}(\varepsilon_{yx}E_x + \varepsilon_{yy}E_y) \end{aligned} \tag{1}$$

where ε_{ij} is the 2D dielectric tensor of the birefringent material. For photoelastic (stress-birefringent) materials, ε_{ij} depends on the 2D stress tensor σ_{ij} and follows the constitutive relation:

$$\varepsilon_{ij} - \varepsilon\delta_{ij} = C_1\sigma_{ij} + C_2\sum_{k=1}^{3}\sigma_{kk}\delta_{ij}. \tag{2}$$

By rotating the x and y axes and diagonalizing, the difference of the principle values of the two tensors can be related in a simplified fashion:

$$\varepsilon_1 - \varepsilon_2 = C_3(\sigma_1 - \sigma_2). \tag{3}$$

Here C_1, C_2 and C_3 are material constants. The angle of this rotation φ defines the *secondary principle axes* (SPA).

Eq. 1 can also be simplified along the SPA. Furthermore, using Eq. 3, we have:

$$\begin{aligned}\frac{dB_1}{dz} &= -\frac{1}{2}iC_0(\sigma_1-\sigma_2)B_1 + \frac{d\varphi}{dz}B_2,\\ \frac{dB_2}{dz} &= -\frac{d\varphi}{dz}B_1 + \frac{1}{2}iC_0(\sigma_1-\sigma_2)B_2\end{aligned} \tag{4}$$

where C_0 is the stress-optic coefficient determined by C_1 and C_2. Here B_i is the mathematical transformation of E_i, the Jones vector along the SPA, and retains its polarization information. In other words, the phase retardation Δ between B_1 and B_2, if solvable from Eq. 4, is the key quantity needed to calculate the final intensity of the outgoing light.

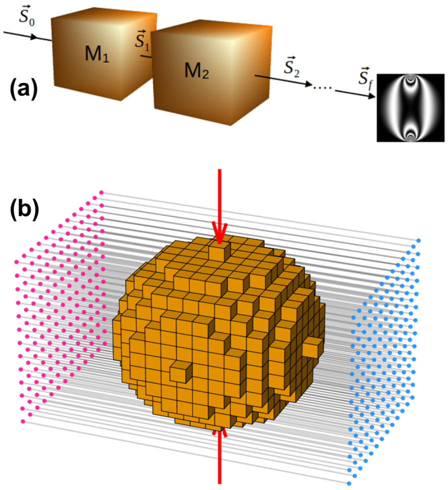

Figure 2. (a) Incident polarised light represented by the Stokes vector S_0 passing through birefringent material divided into voxels. Each voxel represents a uniform stress state and therefore a single Müller matrix M, (b) the discretization of a particle into multiple voxels.

In the 2D case, σ_{ij} is a constant tensor along the light path, which leads to the facts that σ_1 and σ_2 are both constants, while $\frac{d\varphi}{dz} = 0$. Eq. 4 yields the so-called Wertheim Law: $\Delta = C_0(\sigma_1 - \sigma_2)\delta z$, where δz is the distance that the light beam has traveled along z axis, i.e., the thickness of the 2D photoelastic disk.

In the 3D case, σ_{ij} generally changes along the light path. Therefore, $\sigma_1 = \sigma_1(z)$, $\sigma_2 = \sigma_2(z)$, and $\frac{d\varphi}{dz} \neq 0$. To be able to calculate the integrated photoelastic effect, one can divide the light path into small segments. The segment must be small enough such that, within one segment, $\sigma_1 - \sigma_2$ and φ can be considered as a constant and the conditions explained for the 2D system can be utilized here. Given the initial polarization state and the stress distribution within the particles calculated by FEM from the previous section, the change of the polarization state can be calculated in each segment using the Wertheim Law with δz now being the length of the segment. After this calculation in one segment after another until the last one, the final polarization state can then be used to obtain the photoelastic image pixel intensity.

For a more in depth discussion of the theory of integrated photoelasticity, readers should refer to reference [20].

4 Simulation of photoelasticity

Figure 2 (a) illustrates the calculation of the polarization state of two or more segments on the light path in 3D case described in the previous section. Here, instead of using the Jones vector, it is more convenient to adopt the Stokes vector S which has 4 components that completely describe the polarization state.

If $\boldsymbol{S}_{in}$ and $\boldsymbol{S}_{out}$ represent the light beam before and after passing through the segment, the 2D photoelastic effect applicable within the segment can then be described by $\boldsymbol{S}_{out} = \boldsymbol{M} \cdot \boldsymbol{S}_{in}$. The 4×4 matrix $\boldsymbol{M}$ is called the Müller matrix:

$$\boldsymbol{M} = \begin{pmatrix} 1 & 0 & 0 & 0 \\ 0 & \cos^2 2\varphi + \sin^2 2\varphi\,\cos\Delta & (1-\cos\Delta)\,\sin 2\varphi\,\cos 2\varphi & -\sin\Delta\,\sin 2\varphi \\ 0 & (1-\cos\Delta)\,\sin 2\varphi\,\cos 2\varphi & \sin^2 2\varphi + \cos^2 2\varphi\,\cos\Delta & \sin\Delta\,\cos 2\varphi \\ 0 & \sin\Delta\,\sin 2\varphi & -\sin\Delta\,\cos 2\varphi & \cos\Delta \end{pmatrix} \tag{5}$$

M does only depend on the phase retardation Δ and the angle of the SPA φ, as described in the previous section.

$$\Delta = C_1(\delta z)(\sigma_1' - \sigma_2') \tag{6a}$$

$$\varphi = arccos\left(\frac{\bar{v}_1 \cdot \bar{e}_1}{|\bar{v}_1|}\right) \tag{6b}$$

In 3D, they can be calculated in terms of the eigenvalues $\sigma'_{i=1,2}$ and respective eigenvectors $\bar{v}_{i=1,2}$ of a local stress tensor defined as a 2D cross-section of a stress ellipsoid cut by the x-y plane (z axis being the light propagation direction as established in section 3) and $\bar{e}_1$ is a unit vector along its x-axis.

For computing the final Stokes vectors that include the information about the light intensity of that specific light ray, we use a 3D voxel grid as shown in Figure 2 (b). In each of these voxels, we assume a constant state of stress obtained by interpolating the nearest stress tensor values from the FEM results. This discretization allows us to calculate the Müller Matrix for each voxel using Equations 6 and 5. Consecutive multiplication of the Stokes vector with the Müller Matricies of the voxels along one light ray yields the brightness of this ray. This brightness corresponds to the intensity of one single pixel in the final image. By repeating this process for all the rays and combining the pixels, we create a photoelastic image such as the ones shown in Fig. 3.

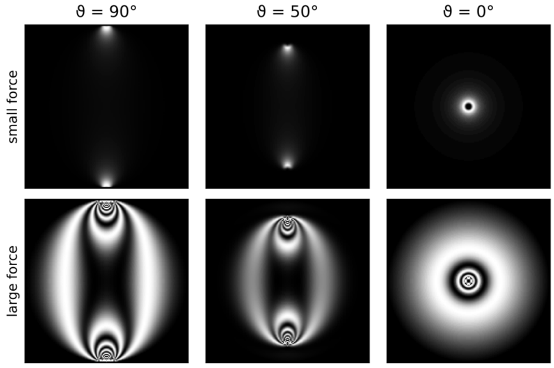

Figure 3. Examples of different images created with our simulation of photoelasticity. The particle is loaded diametrically (as shown in fig. 1) along the polar axis (polar angle $\vartheta = 0°$) and viewed from different ϑ. The top row has a small loading force and no fringe appears, while the bottom row has a larger force leading to visible fringe patterns. Each image has 151^2 pixels and is computed from a grid of 151^3 voxels.

Figure 3 shows that the the FEM simulation described in section 2 allows for an arbitrary choice of the contact force value. This enables us to control the existence and number of fringes in the photoelastic images.

Additionally, by changing the origin and the direction of the rays as well as rotating the voxelized sphere, we can observe the sphere from different viewpoints, as shown in Figure 3, where three different viewpoints (specified by different polar angles ϑ) for two diametric load forces are presented. Here the azimuth angle φ does not affect the outcome.

In summary, using the techniques described in this work, photoelastic images of compressed granular samples can be examined from arbitrary observation angles. By changing the underlying FEM simulation, arbitrary particle configurations can be created. While we only present images created using a circular polariscope, the switch to a linear polariscope setting requires little effort. Besides fulfilling an educational purpose, this framework can be used to train a neural network to solve the inverse problem of recovering the 3D force configurations within the sample, as we will report in a future publication.

References

[1] P. Dantu, A contribution to the mechanical and geometrical study of non-cohesive masses, in *Pros. 4th Int. Conf. Soil Mech. and Found. Eng.* (1957), pp. 144–148

[2] T.S. Majmudar, R.P. Behringer, Contact force measurements and stress-induced anisotropy in granular materials, nature **435**, 1079 (2005).

[3] R. Behringer, D. Bi, B. Chakraborty, A. Clark, J. Dijksman, J. Ren, J. Zhang, Statistical properties of granular materials near jamming, Journal of Statistical Mechanics: Theory and Experiment **2014**, P06004 (2014).

[4] T. Majmudar, M. Sperl, S. Luding, R.P. Behringer, Jamming transition in granular systems, Physical review letters **98**, 058001 (2007).

[5] D. Bi, J. Zhang, B. Chakraborty, R.P. Behringer, Jamming by shear, Nature **480**, 355 (2011).

[6] R. Hartley, R. Behringer, Logarithmic rate dependence of force networks in sheared granular materials, Nature **421**, 928 (2003).

[7] J. Ren, J.A. Dijksman, R.P. Behringer, Reynolds pressure and relaxation in a sheared granular system, Physical review letters **110**, 018302 (2013).

[8] J. Tang, R.P. Behringer, Orientation, flow, and clogging in a two-dimensional hopper: Ellipses vs. disks, Europhysics Letters **114**, 34002 (2016).

[9] N. Brodu, J.A. Dijksman, R.P. Behringer, Spanning the scales of granular materials through microscopic force imaging, Nature communications **6**, 6361 (2015).

[10] R. Hurley, S. Hall, J. Andrade, J. Wright, Quantifying interparticle forces and heterogeneity in 3d granular materials, Physical review letters **117**, 098005 (2016).

[11] C.h. Liu, S.R. Nagel, D. Schecter, S. Coppersmith, S. Majumdar, O. Narayan, T. Witten, Force fluctuations in bead packs, Science **269**, 513 (1995).

[12] P. Yu, S. Frank-Richter, A. Börngen, M. Sperl, Monitoring three-dimensional packings in microgravity, Granular Matter **16**, 165 (2014).

[13] W. Li, R. Juanes, Dynamic imaging of force chains in 3d granular media, Proceedings of the National Academy of Sciences **121**, e2319160121 (2024).

[14] M. Wijerathne, K. Oguni, M. Hori, Stress field tomography based on 3d photoelasticity, Journal of the Mechanics and Physics of Solids **56**, 1065 (2008).

[15] M. Araya-Polo, J. Jennings, A. Adler, T. Dahlke, Deep-learning tomography, The Leading Edge **37**, 58 (2018).

[16] G. Wang, J.C. Ye, B. De Man, Deep learning for tomographic image reconstruction, Nature machine intelligence **2**, 737 (2020).

[17] J.C. Petit, N. Kumar, S. Luding, M. Sperl, Additional transition line in jammed asymmetric bidisperse granular packings, Physical review letters **125**, 215501 (2020).

[18] Abaqus users manual, dassault systèmes simulia corp., Providence, RI, USA. (2023).

[19] R.L. Jackson, I. Green, A finite element study of elasto-plastic hemispherical contact against a rigid flat, J. Trib. **127**, 343 (2005).

[20] H. Aben, Integrated photoelasticity (McGraw-Hill International Book Company, 1979)